

NUMERICAL STUDY OF UNSTEADY EFFECTS IN COMBUSTION SYSTEMS BY MEANS OF COUPLED EXPLICIT ALGEBRAIC REYNOLDS STRESS MODEL (EARSM) AND EXPLICIT ALGEBRAIC SCALAR FLUX MODEL (EASFM)

A. Yun*, A. Sadiki**, J. Janicka**

(*) A. Lyulka Scientific-and-Technical Center, NPO Saturn
13 Kasatkin str., Moscow, 129301 Russia
alex@yun.su

(**) Department of Energy and Power Plant Technology
Technical University of Darmstadt
Petersenstr. 30, 64287, Darmstadt, Germany
sadiki@ekt.tu-darmstadt.de

Abstract

The swirl flow plays a central role in combustion systems. It is important to capture all phenomena associated with it. In particular, lean partially premixed combustion in gas turbine combustion chamber is often associated with hydrodynamic instabilities, known as precessing vortex core (PVC). Therefore an unconfined swirl flow with a precessing vortex core is being studied in presented work by means of simulations and experiments. The ability of explicit algebraic formulation to capture such flow and mixing properties by using economical cost required for engineering design purposes is demonstrated. The experiment has been carried out by Schneider [3] and the first time dependent numerical investigation, based on Reynolds stress models, has been presented by Maltsev [2] and with LES by Wegner [5].

Introduction

For many industrial and engineering purposes statistical modeling will continue to be the main approach to represent the effects of turbulent processes in CFD for technical flows regardless of recent progress in Large Eddy Simulation (LES) and novel development of statistical closures at a level higher than the first order. While first order model provide excellent predictions for many flows of engineering interest, there are many applications for which predicted flow properties differ greatly from corresponding measurements, e.g. flows with sudden changes in mean strain rate, flows over curvature surface, flows with secondary motions, unsteady effect in combustion systems etc. In contrast to the first order models the second order models allow to take into account many effects included to above named flows. Unfortunately, the number of additional transport equations for turbulent quantities of the flow field (Reynolds stress tensor) and the scalar field (scalar flux vector) increased dramatically to 7+3 for second order models from 2+0 for $k-\varepsilon$ models and gradient assumption. Compromise between first and second order models is the nonlinear models, which have strong binding to the calibration of model coefficients by nonlinear terms e.g. CLS model has 7 model coefficients. This can be overcome

by the algebraic formulation resulting from the full Reynolds stress models. Therefore these models save the simplest of models of first level and allow to describe many effects as models of second level.

Governing Equation

The turbulent mean flow of a viscous, incompressible fluid is governed by the Reynolds-averaged continuity and Navier-Stokes equations

$$\frac{\partial \bar{u}_i}{\partial x_i} = 0, \quad (1)$$

$$\frac{\partial \bar{u}_i}{\partial t} + \frac{\partial \bar{u}_i \bar{u}_j}{\partial x_j} = -\frac{1}{\rho} \frac{\partial \bar{p}}{\partial x_i} - \frac{\partial}{\partial x_j} \left(\nu \frac{\partial \bar{u}_i}{\partial x_j} + \tau_{ij} \right) + g_i, \quad (2)$$

where $\tau_{ij} = \overline{u'_i u'_j}$ is the unclosed Reynolds stress tensor and g_i is the gravitation force.

The scalar field is described by a scalar equation of the form:

$$\frac{\partial \bar{\phi}}{\partial t} + \bar{u}_j \frac{\partial \bar{\phi}}{\partial x_j} = \frac{\partial}{\partial x_j} \left(D \frac{\partial \bar{\phi}}{\partial x_j} + Q_j \right) + \frac{1}{\rho} \bar{S}, \quad (3)$$

where $Q_j = \overline{\phi' u'_j}$ is the unclosed turbulent scalar flux and \bar{S} the source term (e.g. chemical reaction). The latter is not considered here. The formulations of closure relations for the Reynolds stress tensor τ_{ij} and the turbulent flux vector Q_j are based on explicit algebraic methodology.

Focused on the anisotropy stress tensor $a_{ij} = \overline{u'_i u'_j} / k - 2/3 \delta_{ij}$ and the turbulent flux vector Q_j , the modeled expressions derived from the parent transport equations from which the transport of Reynolds stress tensor and scalar flux vector have to be removed in keeping the production term.

Assuming weak equilibrium in the parent transport equations the following expressions

$$\left(A_3 + A_4 \frac{P}{\varepsilon} \right) a_{ij} = -A_1 S_{ij} + (a_{ik} \Omega_{kj} - \Omega_{ik} a_{kj}) - A_2 \left(a_{ik} S_{kj} + S_{ik} a_{kj} - \frac{2}{3} \delta_{ij} a_{ik} S_{ki} \right), \quad (4)$$

$$P_{\phi j} - \varepsilon_{\phi j} = - \left(c_{\phi 1} + \frac{1}{2} \frac{k}{\varepsilon k_{\phi}} \overline{u'_k \phi'} \frac{\partial \phi}{\partial x_k} \right) \frac{\varepsilon}{k} \overline{u'_i \phi'} + c_{\phi 2} \overline{u'_j \phi'} \frac{\partial u_i}{\partial x_j} + c_{\phi 3} \overline{u'_j \phi'} \frac{\partial u_i}{\partial x_i} + c_{\phi 4} \overline{u'_i u'_j} \frac{\partial \phi}{\partial x_j}, \quad (5)$$

emerge for the anisotropy tensor and the turbulent scalar flux vector, respectively. The resulting expression for the anisotropy tensor using algebraic formulation [4] is:

$$\begin{aligned} a = & \beta_1 S + \beta_2 \left(S^2 - \frac{1}{3} II_s I \right) + \beta_3 \left(\Omega^{*2} - \frac{1}{3} II_{\Omega} I \right) + \beta_4 (S \Omega^* - \Omega^* S) + \beta_5 (S^2 \Omega^* - \Omega^* S^2) + \\ & + \beta_6 \left(S \Omega^{*2} - \Omega^{*2} S - \frac{2}{3} IVI \right) + \beta_7 \left(S^2 \Omega^{*2} + \Omega^{*2} S^2 - \frac{2}{3} VI \right) + \beta_8 (S \Omega^* S^2 - S^2 \Omega^* S^2) + \\ & \beta_9 (\Omega^* S \Omega^{*2} - \Omega^{*2} S \Omega^*) + \beta_{10} (\Omega^* S^2 \Omega^{*2} - \Omega^{*2} S^2 \Omega^*), \end{aligned} \quad (6)$$

where Ω^* is the curvature corrected vorticity tensor following Girimaji (1997), S the normalized symmetric part of the velocity gradient and

$$\begin{aligned}
II_s &= S^2 = S_{ij}S_{ij}, \quad II_\Omega = \Omega^2 = \Omega_{ij}\Omega_{ji} \\
III &= S^3 = S_{ij}S_{jk}S_{ki}, \quad IV = S\Omega^2 = S_{ij}\Omega_{jk}\Omega, \\
V &= S^2\Omega^2 = S_{ij}S_{jk}\Omega_{kj}\Omega_{jk}
\end{aligned} \tag{7}$$

are invariants. The anisotropy tensor in (6) is written in matrix form. The detailed EARSIM solution can be found in [4]. The unknown model coefficients, β , are determined from (4).

For the turbulent scalar flux it results [6]:

$$-\rho \overline{u'_i \phi'} = -(1 - c_{\phi 4}) B_{ij} \frac{k}{\varepsilon} \overline{u'_j u'_k} \frac{\partial \overline{\phi}}{\partial x_k}, \tag{8}$$

where the tensor B_{ij} is an explicit function of the mean flow gradient normalized by turbulence time scale, the production to dissipation ratio, and the time scale ratio r :

$$B = \frac{\left(G^2 - \frac{1}{2} Q_1 \right) I - G \left(c_s S + c_\Omega \Omega^* \right) + \left(c_s S_{ij} + c_\Omega \Omega^* \right)^2}{G^3 - \frac{1}{2} G Q_1 + \frac{1}{2} Q_2}, \tag{9}$$

where B is written in matrix form and I is the identity matrix. Moreover,

$$c_s = 1 - c_{\phi 2} - c_{\phi 3}, \quad c_\Omega = 1 - c_{\phi 2} + c_{\phi 3}, \tag{10}$$

$$Q_1 = c_s^2 II_s + c_\Omega^2 II_\Omega; \quad Q_2 = \frac{2}{3} c_s^3 III_s + 2c_s c_\Omega^2 IV. \tag{11}$$

Finally

$$G = \frac{1}{2} \left(2c_{\phi 1} - 1 - \frac{1}{r} - \frac{P}{\varepsilon} \right) \text{ with } r = \frac{k_\phi / \varepsilon_\phi}{k / \varepsilon} \approx 0.55. \tag{12}$$

All model coefficients are summarized in Tab. 1.

A_1	A_2	A_3	A_4	$c_{\phi 1}$	$c_{\phi 2}$	$c_{\phi 3}$	$c_{\phi 4}$
1.2	0	1.8	2.25	4.46	-0.5	0.02	0.08

Table 1: Models coefficients.

Application

The swirl burner designed and investigated in [3] is shown in fig. 2. It consists of a 30 mm wide annular slit surrounding a central bluff body of diameter 30 mm. The swirl is generated by a movable block which geometry variations allow to vary theoretical swirl numbers in the range from 0.0 to 2.0. In the experimental investigations and in the present computations the constant swirl number of 0.75 was used. Single point LDV velocity measurements were carried out in [3] at different positions above the burner exit. In addition to the time averaged velocity fields, temporal autocorrelations and power spectral densities were computed from measured samples in order to determine the frequency of PVC.

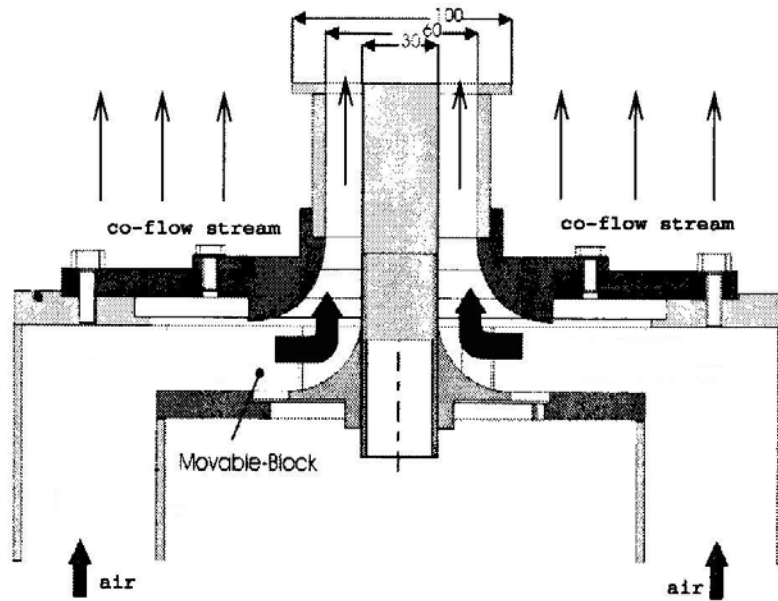


Figure 2: The experimental setup.

The geometrical, numerical and fluid dynamic parameters are summarized in Tab. 2.

Main stream velocity, U_1 , m/s	Co-flow velocity, U_2 , m/s	Re_1 number	CV
1.98	0.5	9310	500000

Table 2: Geometrical and gas dynamic parameters of swirled flows.

The Reynolds number is based on the bulk velocity in the burner exit and the diameter of the bluff body. The computational domain used in the simulation is shown in Fig. 3. The swirl burner is resolved on the computational grid (Fig. 3 left) with 8 radial and 8 tangential channels where inlet boundary conditions are specified. The whole computational domain (Fig. 3 right) consists of the swirl burner and a cylindrical domain of diameter 0.6 m and height 0.72 m. Inlet boundary conditions with constant co-flow velocity $u_c = 0.5$ m/s were specified on the lower face and outlet conditions on the upper face of the cylinder. Free slip (symmetry) boundary conditions were applied to the lateral cylinder boundaries.

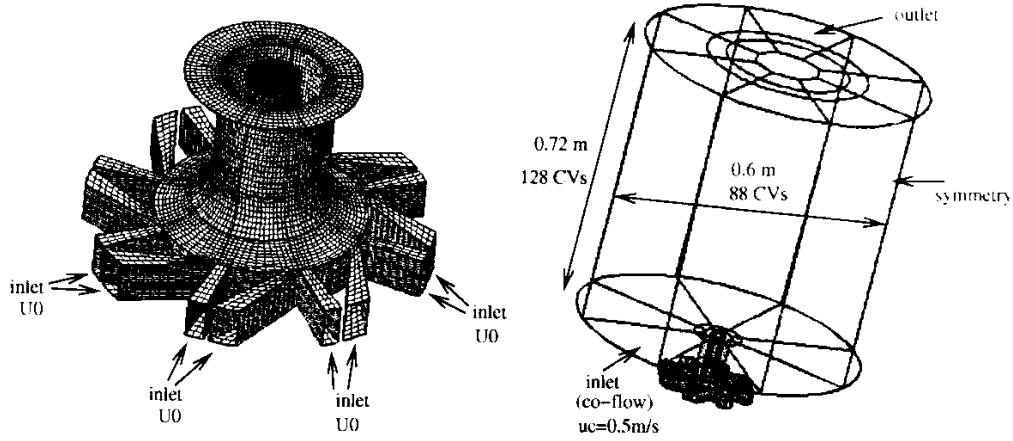


Figure 3: Swirl burner resolved on the computational grid (left) and computational domain (right).

The turbulent quantities (k for $k-\varepsilon$ model and the trace of the Reynolds stress tensor for EARSM computations, respectively) on the inflow boundaries were specified assuming homogeneous isotropic turbulence $k = \frac{3}{2}(u')^2$ with turbulent intensity $T_i = \frac{u'}{U_0} = 0.1$. For the dissipation rate the simplified empirical turbulent

length scale relation $\varepsilon = \frac{k^{3/2}}{l_t}$ was used. Here, the turbulent length scale was assumed to be equal to $l_t = 2$ mm in the swirl inlet boundaries and $l_t = 50$ mm in the co-flow boundary. In order to increase the time accuracy, the time integration was performed with Crank-Nicolson method with constant time step $\Delta t = 5 \cdot 10^{-4}$ within a time-dependent simulation. The flux blending (CDS/UDS mixing) parameters for the convective terms discretisation were $\gamma = 0.9$ for the momentum equations and $\gamma = 0.0$ for all other quantities. Fine grids near burner are used. For $k-\varepsilon$ model the different grids (500000, 700000 and 1000000 CV) have used as well.

Results and discussion

To predict the PVC phenomenon observed in the experiments the URANS technique was applied. Three monitoring points at different radial and axial locations near the burner exit were controlled during simulation. The monitoring points positions were chosen to be the same at which coherent structures were observed in the temporal autocorrelations obtained from the experiments. Provided that high resolution meshes are employed, the calculation with RSM is capable to reproduce the spatial and temporal dynamics of a flow, as demonstrated in [2]. Maltsev (2004) used resolution mesh of 700000, and observed that the computations with $k-\varepsilon$ model could not reproduce any periodicity in the flow investigated here.

In the present work, the ability of EARSM to capture the dynamics of the flow under moderate resolution meshes (see Tab. 2) is asked. The computations with $k-\varepsilon$

model did not exhibit any periodicity with three different meshes (500000, 700000 and 1000000 CV). The velocity signals at the monitoring points changed in time only at the beginning of the simulation while the oscillations were damped and disappeared after a short period of time. The flow field became symmetrical and no PVC could be observed. In the computation with EARSM model, in contrast, a velocity signal harmonically oscillating in time was clearly observed in each monitoring point. For the quantitative analysis of the PVC Fourier transformation of the velocity time series at different selected monitoring points was carried out. The results of such procedure are shown in Fig. 4.

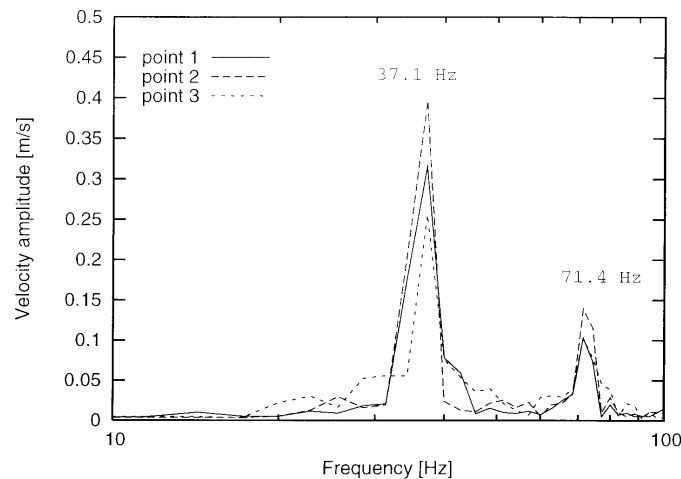


Figure 4: Fourier transformed velocity signal at three spatial points.

Point 1 corresponds to $x = 1mm$, $r = 20mm$, point 2 to $x = 20mm$, $r = 30mm$ and point 3 to $x = 30mm$, $r = 30mm$ positions regarding the burner exit, respectively.

Two obviously dominating peaks at 37.1 Hz and 71.2 Hz in the frequency domain are observed at all three monitoring points. Experimental investigations [3] also found a dominating peak at a low frequency of approximately 38 Hz and a weaker peak at a double frequency. Maltsev [2] found these peaks at frequency 37.1 Hz and 72.6 Hz using RS-models. The presence of the second peak, according to the LES study of Wegner et al. [5], is associated with two small helical vortices opposed to the main vortex core and located in the outside edge of the burner exit. These vortices rotate with the same frequency as the central vortex core. Similarly to velocity it can be observed same dominant frequencies by mixing fraction signal (fig. 5).

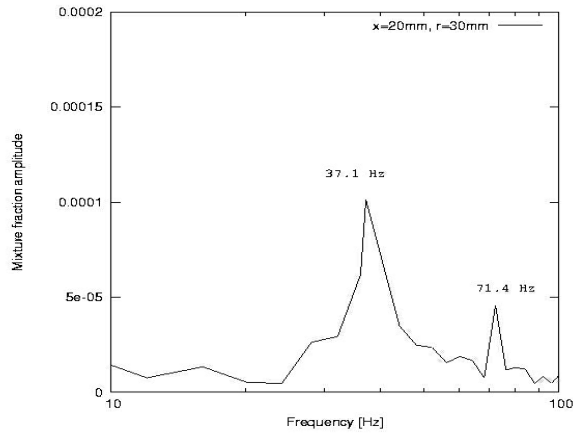


Figure 5: Fourier transformed mixing fraction signal at point to $x = 20mm$, $r = 30mm$ positions regarding the burner exit.

The comparison between RSM, EARSM, $k - \varepsilon$ models and experimental data are summarized in Tab. 3. The Strouhal number is defined as $Str = f \cdot L / U$, where f is the PVC precessing frequency, U , L are the bulk velocity in the burner exit and the diameter of the bluff body respectively.

	<i>1-st freq.</i>	<i>2-nd freq.</i>	<i>Str number</i>
<i>RSM</i>	<i>37.1</i>	<i>72.6</i>	<i>0.24</i>
<i>EARSM</i>	<i>37.1</i>	<i>71.4</i>	<i>0.24</i>
<i>k - ε</i>	<i>0</i>	<i>0</i>	<i>0</i>
<i>Exp.</i>	<i>38</i>	<i>72</i>	<i>0.25</i>

Table 3: Comparison unsteady characteristics by numerical simulation and experimental data.

The energy spectra are shown in Fig. 6 by simulation with EARSM (URANS) and experiments.

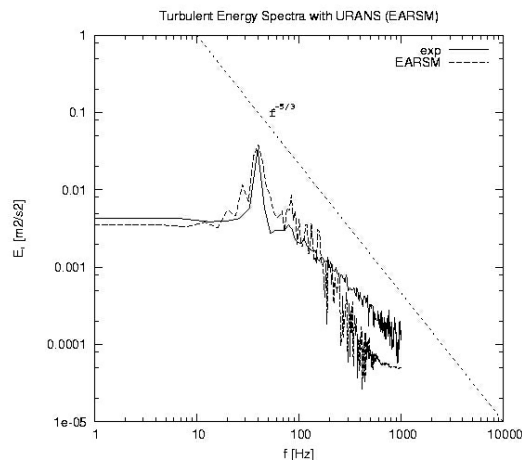


Figure 6: Turbulent energy spectra at the position $x = 1mm$, $r = 20mm$ regarding the burner exit, obtained from experiments and EARSM (URANS).

In Fig. 7 the velocity vector plots taken from the EARSIM computations on a plane orthogonal to the burner symmetry axis at $x = 30\text{mm}$ downstream from the burner exit are shown.

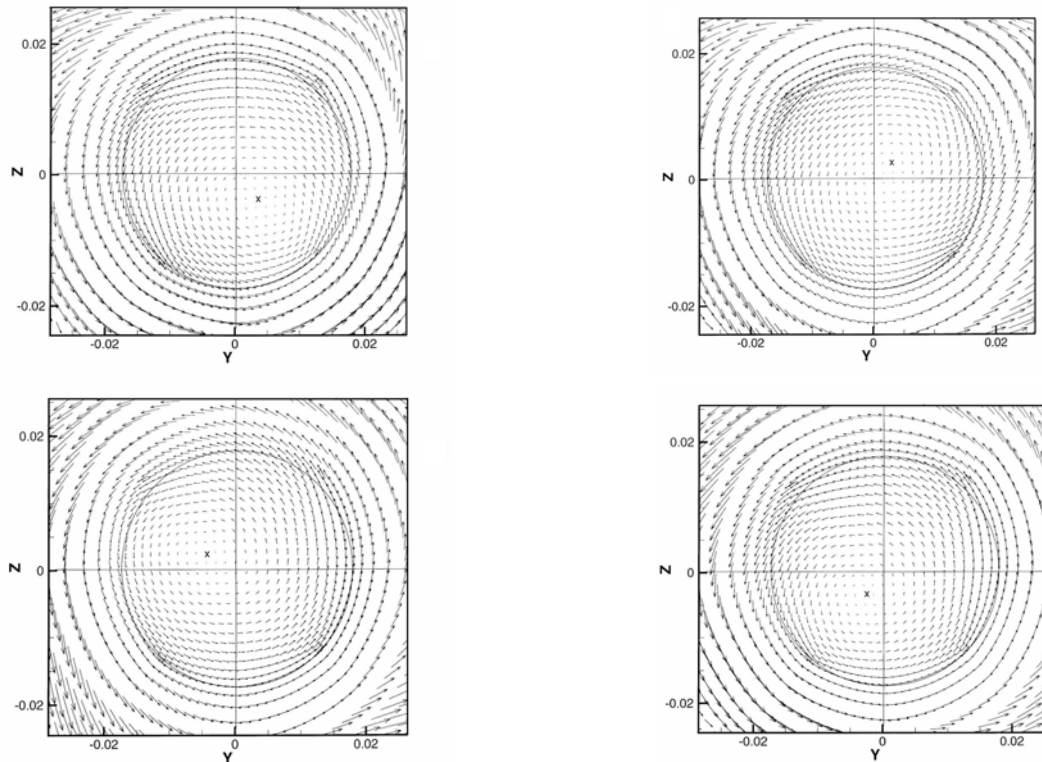


Figure 7: Sequence of snapshots (top left to bottom right) taken on the plane orthogonal to the burner symmetry axis at $x = 30\text{mm}$ downstream from the burner exit.

One can easily distinguish a rotating movement of the vortex center about the burner symmetry axis. The vortex center and the precession direction are also indicated. This flow behavior is known as the PVC.

In Fig. 8, Fig. 9 and Fig. 10 the averaged axial, tangential and radial velocity profiles are shown respectively for different axial positions downstream from the burner exit.

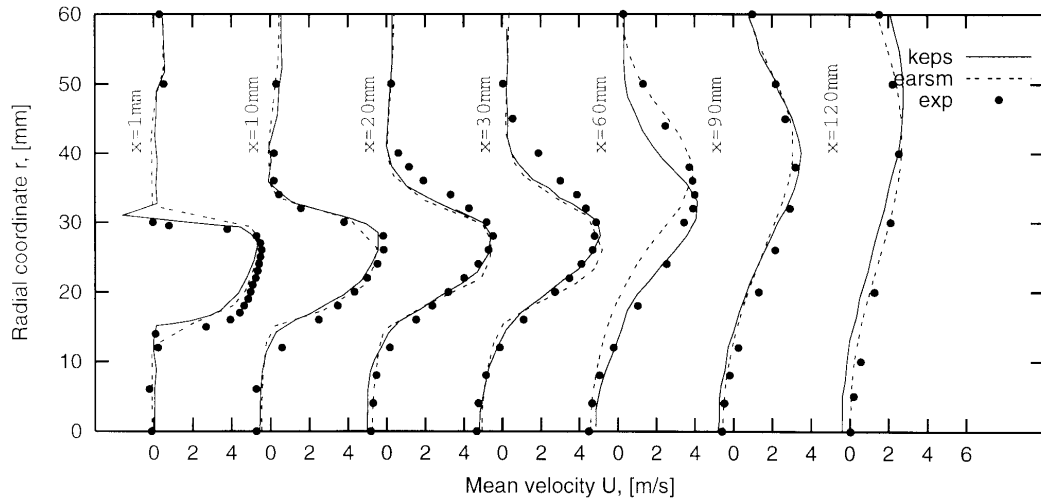


Figure 8: Mean axial velocity at different axial position.

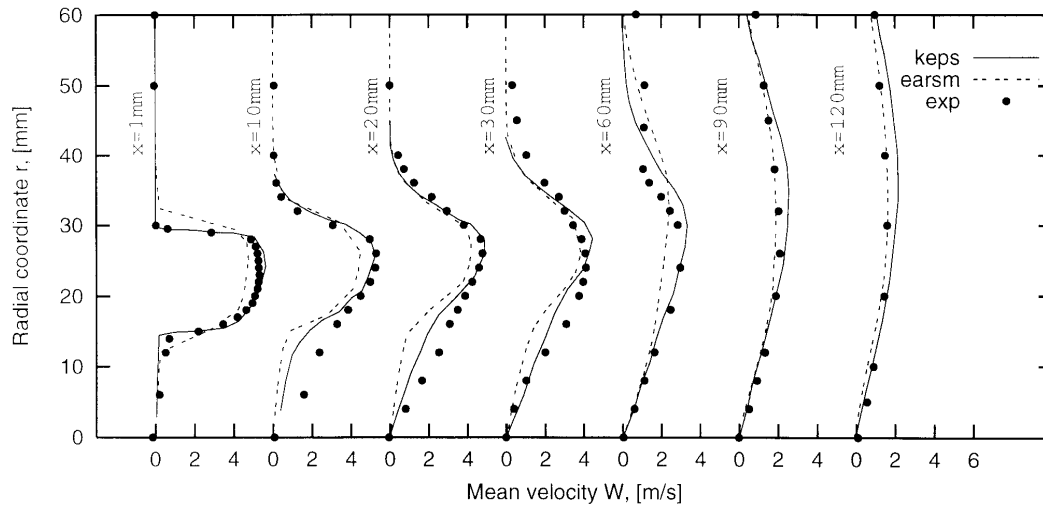


Figure 9: Mean tangential velocity at different axial position.

Good agreement with experimental data is obtained for the burner exit profiles ($x = 1$ mm) by means of both turbulent closures for the mean axial and tangential velocity components (Fig. 8, Fig. 9). The same observations remain true up to ($x = 60$ mm) where a small advantage of EARSM becomes obvious. Further profiles ($x = 90$ mm and $x = 120$ mm) demonstrate that the $k - \varepsilon$ model overestimated the width of the recirculation zone while the EARSM is still able to capture the measured flow structure for both velocity components.

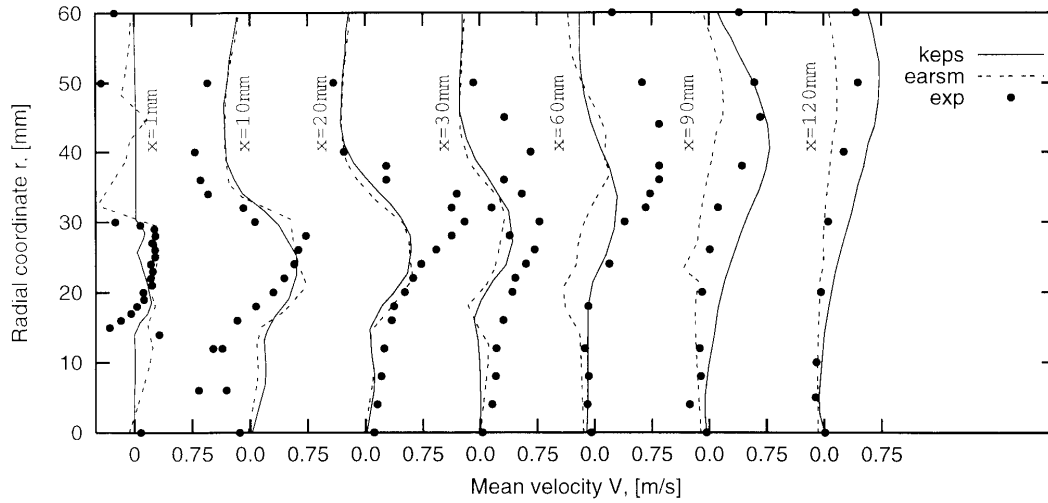


Figure 10: Mean radial velocity at different axial position.

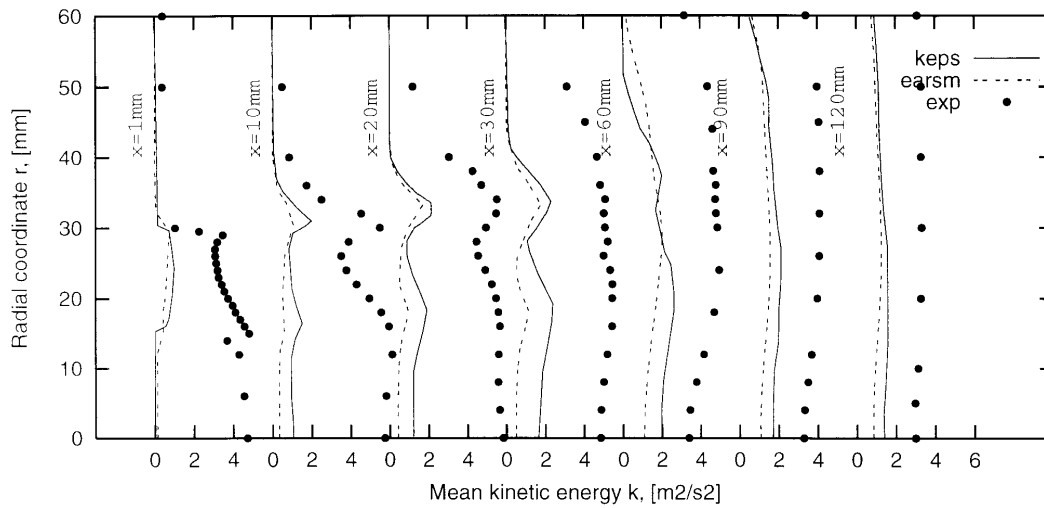


Figure 11: Mean kinetic energy at different axial position.

The situation with the radial velocity and the turbulent kinetic energy is different. The agreement at the burner exit plane (Fig. 10, $x = 1$ mm) for the radial velocity is rather bad for both turbulence models. The same picture (Fig. 11, $x = 1$ mm) is for the turbulent kinetic energy. At axial positions further downstream, however, the level of predicted k becomes nearly the same by means of both turbulence models. The disagreement of EARSM and $k - \varepsilon$ model results may be explained by the underprediction of the amplitude of the coherent oscillations. Unfortunately, it was not possible to extract this amplitude from the experimental data in order to confirm or contradict this supposition. It should be mentioned that the velocity signal amplitude was strongly dependent on the accuracy of the spatial discretisation. Performing the URANS computations with EARSM, for the pure UDS discretisation (flux blending parameter $\gamma = 0$) of the convective terms in the momentum equations the same PVC frequency was predicted as with $\gamma = 0.9$, but the amplitude of the coherent oscillations was significantly smaller than that predicted

with $\gamma = 0.9$. This fact reveals the importance of the numerical accuracy in the prediction of the coherent motion. The values of the radial velocity are captured with reasonable agreement with both EARSM and $k - \varepsilon$ model. Though the measured data for such small mean velocity values (nearly zero) at such a high level of turbulence should be considered very carefully.

Conclusion

The numerical study of a non-confined isothermal swirled flow induced by a swirl burner revealed the complete inability of the linear eddy viscosity ($k - \varepsilon$) formulation to even qualitatively capture a swirl flow instability (PVC) by means of transient computations. The EARSM based turbulence closure was, in contrast, able to obtain the harmonic oscillations with nearly constant (in time) amplitude. The quantitative comparison with experimental results has demonstrated the remarkably accurate prediction of the precession frequency by means of the EARSM approach. The predicted amplitude of the harmonic oscillations was strongly influenced by the spatial discretisation of the convective terms in the momentum equations. This amplitude was, however, underpredicted even with numerical scheme of the highest possible accuracy. This underprediction caused, in turn, the underprediction of the whole fluctuating energy with deviation of even 100% at some flow locations. Unfortunately, for present configuration the unsteady effects has not been captured by $k - \varepsilon$ model with grid refinement as in [1]. Further investigations by $k - \varepsilon$ model are necessary for this reason.

Reference

1. Johmann P., Sinigersky A., Hehle M., Schäfer O, Koch R. *Numerical Simulation of a Precessing Vortex Breakdown*. Elsevier, 2004.
2. Maltsev A. *Towards the Development and Assessment of Complete CFD Models for the Simulation of Stationary Gas Turbine Combustion Processes*. Doctor thesis. Darmstadt. 2004.
3. Schneider C. *Über die Charakterisierung von Turbulenzstrukturen in verdrallten Strömungen*. PhD thesis, Darmstadt, 2003.
4. Wallin S. *Engineering turbulence modeling for CFD with a focus on explicit algebraic Reynolds stress models*. Doctoral thesis. Norstedts Truckeri, Stockholm, Sweden, 2000.
5. Wegner B., Maltsev A., Schneider C., Dreizler A., Sadiki A., Janicka J. *Evaluation of URANS performance in Predicting an Unconfined Swirling Flow with Precessing Vortex core based on LES and Experiments*. Third International Symposium on Turbulence and Shear Flow Phenomena, TSFP3, Sendai, Japan, vol. 1, pp. 51-56, June 25-27, 2003.
6. Wikstrom P.M., Wallin S., Johansson A.V. *Derivation and investigation of a new explicit algebraic model for the passive scalar flux*. *Phy. Fluids*. 12:688-702. 2000.